Selective rubidium recovery from seawater with metal-organic framework incorporated potassium cobalt hexacyanoferrate nanomaterial

Dai Quyet Truong[a], Youngwoo Choo[a], Nawshad Akther[a], Sharaniya Roobavannan[a], Ahmad Norouzi[b], Vipul Gupta[b], Michael Blumenstein[c], Tien Vinh Nguyen[a,*], Gayathri Naidu[a,*]

[a] School of Civil and Environmental Engineering, University of Technology Sydney (UTS), City Campus, Broadway, NSW 2007, Australia

[b]Australian Centre for Research on Separation Science (ACROSS), School of Natural Sciences, University of Tasmania, Hobart, Tasmania 7001, Australia

[c]Australian Artificial Intelligence Institute, Faculty of Engineering and IT, University of Technology Sydney, Sydney, Australia

*Corresponding author(s): Email: Gayathri.Danasamy@uts.edu.au (G. Naidu); Tien.Nguyen@uts.edu.au (TV Nguyen)

Abstract

Rubidium (Rb) is a highly priced metal due to its scarcity in ore form. Seawater is a promising alternate source for recovering Rb. Potassium copper hexacyanoferrate (KCoFC) ion exchange nanomaterial achieves high selective Rb recovery in seawater, however, high potassium in seawater impairs its performance. To overcome this drawback, this study manipulated the structure of KCoFC by grafting zeolitic imidazole frameworks (ZIF) with KCoFC, synthesizing KCoFC@ZIF. Detail physicochemical characterization analysis showed the successful synthesis of KCoFC@ZIF. KCoFC@ZIF increased the materials surface area but reduced the pore diameter and this was influenced by 2-methylimidazole (HMIM) concentration. Reducing HMIM composition to a ratio of KCoFC:HMIM:Zn 1:12:5 (KCoFC@ZIF(d)) achieved a reasonable balance in increasing the material surface area by 63% to that of KCoFC while reducing the pore diameter by only 30%. Rb uptake capacity of KCoFC@ZIF(d) (Langmuir Q_{max} 1279.35 mg/g), was 8-folds higher with accelerated kinetics compared to KCoFC (Q_{max} 143.31 mg/g). In seawater, both KCoFC and KCoFC@ZIF(d) exhibited about 45% capacity reduction due to the presence of potassium. Nevertheless, due to KCoFC@ZIF(d)'s high Rb selective capacity, it was still able to

maintain a relatively high Rb uptake of 236 mg/g in seawater, highlighting its feasible application for Rb extraction in seawater. KCoFC@ZIF(d) enabled to maintain closely similar peak structure after five consecutive operative cycles, establishing the materials regenerative efficiency. Overall, it can be indicated that KCoFC@ZIF's selective Rb uptake is controlled by KCoFC while grafted ZIF layer acts as a catalytic layer that increases the surface area and ion dehydration to enhance Rb diffusion into the core structure of KCoFC.

Keywords

Rubidium; Zeolitic imidazole framework; Nanomaterial; Potassium cobalt hexacyanoferrate; seawater

Introduction

Rubidium (Rb) is a highly priced metal, which can be used in fiber optics, laser technology and telecommunication. The high price of Rb (USD 14720/kg), compared to metals in high demand like lithium (Li, USD 10/kg) [1], is attributed to the rarity of recovering Rb in land mining form. Land mining does not yield Rb as an element in its pristine form. Instead, it is found as a fraction of various ores like lepidolite ($KLi_2Al(Al,Si)_3O_{10}(F,OH)_2$), pollucite, muscovite ($KAl_2[AlSi_3O_{10}](OH)_2$), zinnwaldite ($KAl(Fe,Li)(Si_3Al)O_{10}F_2$), Li mica containing approximately 3.5% Rb_2O, and $(Cs,Na)_2Al_2Si_4O_{12}.2H_2O$ containing iron, potassium and calcium with approximately 1.4% Rb_2O [2, 3]. Therefore, recovery of Rb requires several intricate steps involving precipitation, evaporation and crystallization.

The challenges to recovering Rb in land ore form have motivated Rb recovery from alternative water sources, such as salt lakes, seawater and its related brine [4-7]. Although Rb concentration is low in seawater (0.18 - 0.20 mg/L), due to the extensive and renewable amount of seawater, the total amount of Rb in seawater (~2.5×10^{11} tonnes) exceeds that of land ores [4, 8]. Another attractive aspect of Rb recovery from seawater is that it is comparatively more sustainable than the environmentally detrimental Rb rock mining, which requires complex mechanical and chemical processes. Moreover, the recovery of economically valuable Rb from seawater desalination brine before being directed back to the ocean may provide additional revenue to offset brine treatment costs [5].

Various kinds of inorganic nanomaterials have been evaluated for selective recovery of alkali metal from brine, such as prussian blue [9], natural zeolite [10], potassium metal hexacyanoferrate [11, 12], mesoporous silica [13] and titanium silica [14]. In this regard, the high-performance capacity of potassium metal hexacyanoferrate for maintaining selective Rb recovery over other major ions in high salinity seawater brine has been well established [5, 11, 12]. In a previous study using potassium cobalt hexacyanoferrate (KCoFC) nanomaterial, Naidu et al. [11, 12] attributed the high Rb selective capability to the ion exchange mechanism between Rb that can penetrate the crystal lattice of KCoFC and displace potassium (K) in the lattice, as these two ions have closely similar ionic radii. Nevertheless, one of the main drawbacks here is the significant reduction of Rb sorption in the existence of K because of the ion saturation effect. For example, Naidu et al. [11] reported a significant reduction in Rb sorption by 65-70% with seawater brine compared to model Rb solution due to the high presence of K over Rb (Rb: K molar ratio = 1: 7700) in brine. It is essential to mitigate this limitation to make Rb recovery with KCoFC an economically feasible option.

Manipulating the structure and surface of KCoFC could potentially enhance and maintain a high selective capacity for Rb recovery from seawater in the presence of K. Grafting metal-organic frameworks (MOFs) to KCoFC may offer the potential to manipulate the nanomaterial structure. This is because nanoporous MOFs offer extremely diverse and flexible structures depending on the metal ions and organic linkers that are used to coordinate them. In this regard, previous studies have explored the application of nanomaterial grafting with MOFs for enhancing the recovery of alkali metals, such as Li and Rb. Park et al. [15] fabricated copper phosphonate MOF-alginate nanomaterial and attributed its functional groups to attaining higher Li recovery. In another study, Tian et al. [16] reported the favourable and rapid selectivity of Rb in an aqueous solution by synthesizing carboxymethyl cellulose Fe_3O_4 nanomaterial with zeolitic imidazolate frameworks (ZIF) MOF. Specifically, the usage of ZIF MOFs for enhancing ion transportation in nanomaterials and nanochannels of membranes has been attributed to its versatile manipulation capacity, stability and narrow pore size cavities of ZIF (range of 5-10 Å) that closely matches that of alkali metals like Li and Rb [16, 17]. ZIF is in the category of microporous MOF that is composed of zinc metal clusters with ligands of 2-methylimidazole (HMIM) as binding organic linkers [18-20]. The

composition of ZIF with a strong 145° binding angle between the organic linker and metal cluster mimics the same morphology of oxygen and silica in aluminosilicate natural zeolites. Therefore, in many ways, ZIF shares similar cage-like morphology and structure to natural zeolite with additional benefits of MOF features, such as significantly high surface area and tunable pore size. The potential of grafting ZIF with KCoFC (KCoFC@ZIF) to increase its selective adsorption capacity has not been explored to date. By combining KCoFC with ZIF, it is anticipated that KCoFC nanomaterial could possess properties with high surface area, ultrahigh porosity through ordered crystalline pores and tunable pores, structural flexibility and adaptivity. These characteristics are anticipated to maintain high Rb selectivity in the presence of K.

Hence, this study aims to fabricate a hybrid MOF nanomaterial with ZIF and KCoFC (KCoFC@ ZIF) to increase Rb selective capacity in the presence of K in seawater compared to conventional KCoFC. Several different synthesis methods were carried out to identify the optimum composition of KCoFC@ZIF. An in-depth structure and chemical characterizations were carried out to verify the synthesized nanomaterial. Factors that influence the performance of the produced KCuFC@ ZIF for Rb recovery were examined and a detailed study was carried out on the capacity of KCoFC@ZIF for selective recovery of Rb from seawater. The performance trend and characterization analysis of the nanomaterial were used to build an insight into the mechanism of KCoFC@ZIF towards selective Rb recovery. The feasibility of recovering Rb with KCoFC@ ZIF was established by multiple reuse/regenerative tests.

2. Material and methods

2.1 Chemicals

2.1.1 Synthesis of potassium cobalt hexacyanoferrate, KCoFC

Potassium cobalt hexacyanoferrate (KCoFC) was synthesized in the laboratory according to the procedure mentioned in our prior study [12]. First, 50 mL of 0.5 M potassium ferrocyanide trihydrate ($K_4Fe(CN)_6{\cdot}3H_2O$) was stirred with 120 mL of 0.3 M cobalt nitrate hexahydrate ($Co(NO_3)_2{\cdot}6H_2O$) for an hour at room temperature (25±1^{o}C). Then, the mixture was centrifuged and washed three times with deionized water. Lastly, it was placed overnight in an oven at 115 °C to obtain dried KCoFC material. All chemicals used in this study were analytical grade and procured from Merck Chemical Co., Germany.

2.1.1 Synthesis of KCoFC@ZIF nanomaterial

The prepared KCoFC was ground and sieved to obtain particle size between 0.3 mm to 0.45 mm. Zinc nitrate hexahydrate ($Zn(NO_3)_2 \cdot 6H_2O$) and 2-methylimidazole (HMIM) from Merck Chemical Co. (Germany) were used to synthesize KCoFC@ZIF nanomaterial using the synthesis protocol reported by Min et al. [18]. First, a certain amount of HMIM was added to a 250 mL beaker containing a desired quantity of the synthesized KCoFC with 50 mL ethanol and stirred for 10 min at room temperature. Then, zinc nitrate hexahydrate was incorporated to the mixture and mixed for 1 hr. The synthesized KCoFC@ZIF contained a molar ratio of KCoFC: HMIM: $Zn(NO_3)_2.6H_2O$ of 1 : 30 : 5. Next, the mixture was centrifuged for 20 min at 8000 rpm to collect the solid material, which was then washed with ethanol three times, and placed in an oven at 85 °C to dry overnight.

2.1.1.1 Influence of HMIM concentration on KCoFC

In order to study the influence of HMIM on KCOFC, apart from the KCoFC: HMIM: $Zn(NO_3)_2 \cdot 6H_2O$ of 1 : 30 : 5 (for simplicity this composition is referred to as KCoFC@ZIF(a)), several ratios of KCoFC: HMIM: $Zn(NO_3)_2 \cdot 6H2O$ at different HMIM concentration were synthesized (**Table 1**) and evaluated in detail.

Table 1 Synthesis of KCoFC@ZIF with different doping amount HMIM organic functional group

Nanomaterial label	KCoFC : HMIM : $Zn(NO_3)_2.6H_2O$ ratio	KCoFC (mmol)	HMIM (mmol)	$Zn(NO_3)_2.6H_2O$ (mmol)
KCoFC@ZIF(a)	1 : 30 : 5	1	30	5
KCoFC@ZIF(b)	1 : 50 : 5	1	50	5
KCoFC@ZIF(c)	1 : 20 : 5	1	20	5
KCoFC@ZIF(d)	1 : 12 : 5	1	12	5
KCoFC@ZIF(e)	1 : 8 : 5	1	8	5

2.1.2 Solutions

RbCl, KCl, $CaCl_2$, $MgCl_2$, and NaCl analytical grade chemicals were purchased from Merck Chemical Co. (Germany). Stock solutions of 1000 mg/L Rb, K, Ca, Mg, and Na were prepared

separately by dissolving the chloride salts in Milli-Q water. The solutions for experiments were prepared from dilution of these stock solutions.

2.2 Characterization methods

The crystalline structures of KCoFC and KCoFC@ZIF materials were characterized by X-Ray diffractometer (Bruker D8 Discover) using Cu Kα radiation. The powder sample was collected and scanned at a resolution of 0.04 °/s in the 2θ range from 5° to 50°.

The surface morphology of KCoFC and KCoFC@ZIF nanomaterials were investigated using scanning electron microscopy (SEM, Zeiss Supra 55VP) with an acceleration voltage of 10 kV both before and after the Rb adsorption process. Samples were thoroughly dried under an active vacuum for 12 hours to remove all the residual solvent prior to the characterization. The samples were sputter coated with Au/Pd alloy with 10 nm thickness to suppress the charging on the surface. Energy dispersive X-ray spectroscopy (EDX) was utilized to investigate the elemental composition of the nanomaterials using an X-ray detector (Oxford Instruments). Transmission electron microscopy (TEM, FEI Tecnai G2 20, 200 kV) was performed to resolve the interfacial structure and elemental composition of the composite particles. Powder samples were dispersed in DI water followed by shaking in a 1.5 mL Eppendorf tube. Supernatant of the solution was collected by micropipette and a droplet of the solution was applied on a Formvar supported TEM grid. The specimen was thoroughly dried in a vacuum oven maintained at 80 °C overnight to remove moisture.

Nitrogen adsorption-desorption on KCoFC@ZIF material was investigated using a BET surface area analyser with nitrogen as the gaseous adsorbate (Micromeritics TriStar II Plus, Australia). The specific surface area (S_{BET}) was evaluated by employing the standard Brunauer–Emmett–Teller (BET) method. The total pore volume (V_{total}) was anticipated to be the liquid nitrogen volume at a relative pressure (P/P_0) of about 0.99. The average pore diameter was calculated using **Eq. 1** [12]:

$$D = 4V_{total}/S_{BET} \quad (1)$$

Fourier transform infrared spectrometry (FT-IR, MIRacle 10, Shimadzu) was employed with a scan range of 4000 – 600 cm^{-1} to analyze the chemical composition and functional groups of the synthesized KCoFC and KCoFC@ZIF materials.

Zeta potential analysis was carried out to assess the surface charge of the nanomaterials in a pH range of 2 to 10 with 1 $x10^4$ M NaCl as background electrolyte solution. The zeta potential value was assessed using a Zetasizer nano instrument (Malvern, UK).

2.3 Batch performance evaluation of nanomaterials for Rb uptake

All experiments were performed following a uniform procedure. First, a known amount of nanomaterials were weighed and placed into a set of conical glass flasks. Model solutions (100 ml volume, 5 mg/L Rb unless mentioned otherwise) were then added to flasks. The flasks were shaken at 120 rpm for 24 h in a shaker at room temperature (24 ± 1 °C). The shaking time was set to 24 h to ensure equilibrium state of Rb uptake. At the end of 24h, solution samples from each flasks were collected in falcon tubes and filtered through a 1.2 µm syringe membrane filter to remove the residual particles. The ion concentration in the sample solutions were measured through inductively coupled plasma mass spectrometry (ICP-MS, Agilent 7900, Agilent Technologies, Inc.).

2.3.1 Influence of pH

The effect of initial pH and zeta potential in the solution on Rb sorption was studied in a pH range of 2 to 10. The initial pH value of each solution was set by using 0.1 M NaOH and 0.1 M HCl standards. Next, 0.025 g KCoFC@ZIF were added to each flask and the suspensions were shaken. The pH values before and after the sorption time were recorded with a pH meter (HQ40d, Hach).

2.3.2 Kinetics study

Rb uptake kinetics experiment was performed in a collection of glass flasks comprising 100 mL of Rb solution (5.0 mg/L) and pH of 7.0 ± 0.5 with a nanomaterial dosage of 0.05 g/L. The samples were gathered at various time intervals from 15 min to 24 h and the Rb concentration was measured after filtering the samples. The Rb uptake at time t (q_t) was calculated using Eq. 2:

$$q_t = \frac{(C_0 - C_t) \cdot V}{m} \quad (2)$$

where C_0 (mg/L) is the initial Rb concentration in the solution, C_t is the Rb concentration in the liquid phase at time t, m is the nanomaterial amount (g) and V is the solution volume (L).

The obtained data were fitted using the pseudo-first-order (PFO) and pseudo-second-order (PSO) kinetic models as described by Eq. 3 [21] and Eq. 4 [22], respectively:

$$q_t = q_e \cdot \left(1 - e^{-k_1 t}\right) \quad (3)$$

$$q_t = \frac{k_2 q_e^2 t}{1 + k_2 q_e t} \quad (4)$$

where t (min) is the contact time, q_t (mg/g) is the Rb uptake per unit mass of nanomaterial at t, q_e (mg/g) is the q_t value at equilibrium state (mg/g), k_1 (min^{-1}) and k_2 (g/mg·min) are the rate constants of PFO and PSO expressions, respectively.

2.3.3 Isotherm study

The performance of nanomaterials for Rb uptake was represented by batch isotherm evaluation. Experiments were conducted using a Rb model solution (100 mL, 5 mg/L) with variable nanomaterial dosages ranging from 0.01 to 0.25 g/L. An optimum pH was used upon identifying the optimum pH value. At the equilibrium state, the sorption capacity (q_e) was determined by Eq. 5:

$$q_e = \frac{(C_0 - C_e) \cdot V}{m} \quad (5)$$

where C_0 and C_e are the initial and equilibrium concentrations of Rb in the solution (mg/L), m is the amount of nanomaterial (g) and V is the solution volume (L).

To investigate the isotherm characteristics of the sorbent, the experimental data was applied to Langmuir [23] (Eq. (6) and Freundlich [24] (Eq. (7) empirical equations:

$$q_e = \frac{K_L.q_{max}.C_e}{1 + K_L.C_e} \quad (6)$$

$$q_e = K_F C_e^{1/n} q_e \quad (7)$$

where q_e (mg/g) is the Rb uptake capacity at equilibrium, K_F ((mg/g)/(mg/L)$^{1/n}$) is Freundlich capacity factor; K_L (L/mg) is Langmuir constant, q_{max} (mg/g) is the maximum Rb uptake capacity of the nanomaterial at equilibrium, *1/n* is Freundlich intensity parameter, and C_e (mg/L) is the equilibrium concentration of Rb in aqueous solution (mg/L).

2.4 Selective Rb uptake from seawater

The performance and selectivity of the synthesized KCoFC and ZIF grafted KCoFC towards Rb uptake over other major cations present in seawater were investigated using actual seawater solution. The seawater characteristics and major cations are shown in **Table 2**. For direct comparison with the model Rb solution and reasonable ICP-MS ion measurement of the sample, the seawater was spiked with 5 mg/L of Rb.

Table 2 Composition of seawater

Parameter	Value
Total dissolved solids (mg/L)	35000
pH	7.1
Inorganic cations (mg/L)	
Ca	416.8
Mg	1357.3
Na	11837.6
K	373.6
Rb	0.2

2.5 Regeneration and reuse

To investigate the reuse potential of the saturated materials, a series of regeneration tests were conducted. Firstly, batch adsorptions were carried out with Rb model solution and 0.1 g/L dose of KCoFC and KCoFC@ZIF nanomaterials. After the adsorption process reached an equilibrium state (24 h), the solid materials were filtered through 0.45 μm filter paper, and, dried at room temperature. In the following stage, batch desorption process was carried out in which, the exhausted sorbents were mixed with 50 mL of 1.0 M KCl for 30 min stirring. Thereafter, the materials were filtered and dried at 50 ^{o}C until the constant mass to obtain the regenerated material. The process of adsorption-desorption was repeated for five consecutive cycles. The Rb concentration in the liquid phase after each adsorption test was determined and compared between the original and the regenerated sorbents to establish the regenerative performance of KCoFC and KCoFC@ZIF nanomaterials.

3. Results and discussion

3.1 Synthesis of metal-organic framework ZIF with KCoFC

Metal-organic framework ZIF with KCoFC was synthesized in the lab, by a step-by–step method as illustrated and described in **Figure 1**. First, neat potassium cobalt hexacyanoferrate ($K_2[CoFe(CN)_6]$, KCoFC) particles were synthesized by mixing the precursors, i.e., potassium ferrocyanide trihydrate, and cobalt nitrate hexahydrate in DI water. The resulting product appeared as a dark brown colored powder (**Figure 1**). ZIF crystals were synthesized by a facile in situ synthesis method in an ambient aqueous condition ([18]). The neat KCoFC particles were well dispersed in an aqueous solution of a certain concentration of HMIM. Stirring the KCoFC/HMIM mixture for 10 mins promoted the association of the imidazole group on the surface of KCoFC particles. Subsequently, a certain amount of zinc nitrate was added and the solution was stirred for 1 h to form KCoFC@ZIF composite particles. Typically, the crystallization of the ZIF occurs fast and the structure and porosity of the crystals are stable by 50-60 mins of the synthesis time [25]. Hence, we terminated the ZIF synthesis reaction at 60 mins. Therefore the mixed material was centrifuged and washed with ethanol to removal the unreacted precursors and free-standing ZIF particles. The final product of the composite particles showed closely similar physical appearance to the neat KCoFC (**Figure 1**). Previous studies report successful in-situ growth of the ZIF crystals on polar substrates such as graphene oxide sheets or layered double hydroxides [26, 27]. Given the highly polar nature of the KCoFC surface, the in situ growth of ZIF crystal on KCoFC is expected to be feasible and warrants chemical stability in ambient conditions.

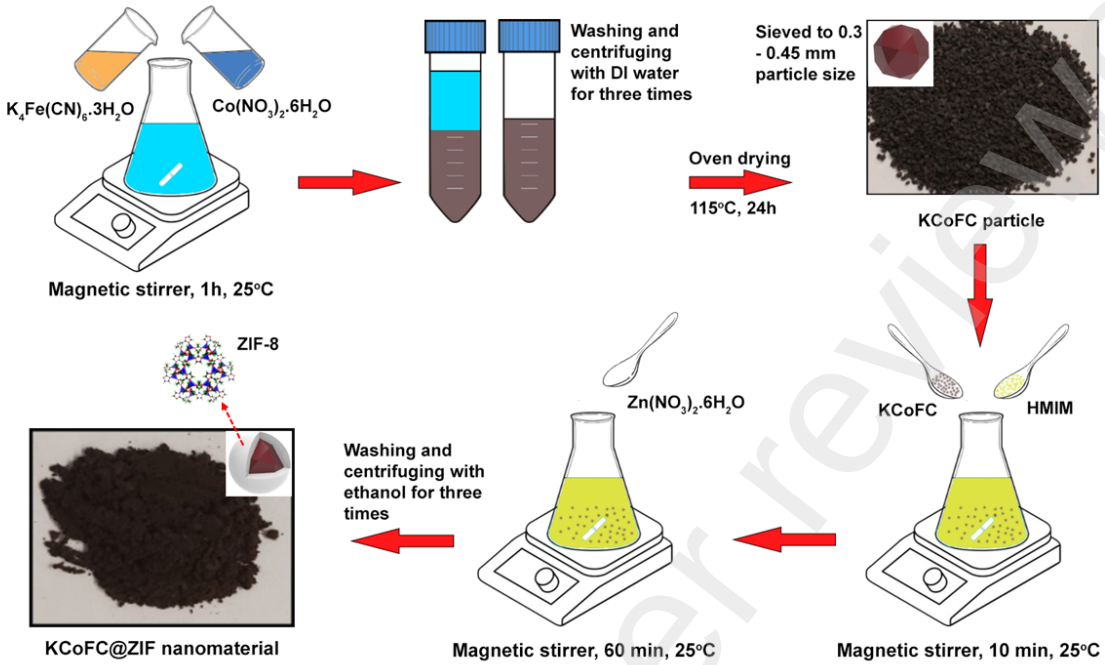

Figure 1. Lab synthesis procedure of KCoFC@ZIF nanomaterial

3.2 Materials characterization

3.2.1 Crystal Structures of the KCoFC and KCoFC@ZIF

Crystal structures of the KCoFC and ZIF-grafted KCoFC composite nanoparticles (KCoFC@ZIF(a)) were characterized by X-ray diffraction (**Figure 2**). The sharp characteristic peaks of the neat KCoFC appeared at 17.7°, 25.1°, 35.8°, 40.1°, and 44.1° which are assignable to the (200), (220), (400), (222), and (422) planes of the KCoFC crystal, respectively. The peak positions are consistent with the literature confirming the face-centered cubic lattice structure was formed in neat KCoFC particles [12, 28, 29]. The XRD pattern of KCoFC@ZIF(a) showed additional peaks appeared at 7.4°, 10.4°, and 12.8° which are attributed to the (110), (200), and (211) reflections of ZIF crystals, respectively, suggesting that the ZIF crystals successfully formed in the composite. The KCoFC peaks were well-maintained, specifically, no peak shifts or peak broadening was observed, after the encapsulation of the ZIF layer indicating that the crystalline structure of the KCoFC was unaffected during the ZIF growth.

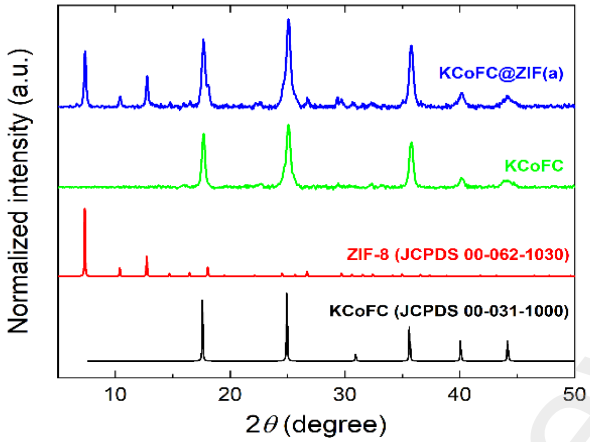

Figure 2. Powder XRD patterns of KCoFC and ZIF-grafted KCoFC (KCoFC@ZIF(a)).

3.2.2 Surface morphology and elemental composition

Figure 3 (a) shows an SEM micrograph of a neat KCoFC particle. A globular microporous structure with an average diameter of ~10 nm was observed on the surface of neat KCoFC particles. The KCoFC@ZIF composite particle shown in **Figure 3 (b)** demonstrates structural similarity with the undecorated particles, however, the size of the globular structure appears to be bigger than the neat KCoFC indicating that the ZIF crystals were formed on the surface of the core KCoFC particles. The average size and shape of the decorated ZIF-8 particles are in good agreement with the reported values which utilized similar synthesis parameters [25]. To identify the ZIF particles on the exterior of the KCoFC, EDX analysis was performed (**Figure 3 (c), (d)**). The results indicate that the KCoFC particles contain cobalt, iron, and potassium, whereas the KCoFC@ZIF(a) composite particle exhibits an additional zinc signal confirming the formation of ZIF phase on the surface. (**Figure 3 (e), (f)**)

Although SEM-EDX analyses demonstrate the presence of zinc content in the composite particles, the interfacial structure of the composite particles was not clearly resolved. To investigate the interfacial structure and confirm the direct growth of ZIF crystals only on the surface of KCoFC, TEM-EDX was performed on the composite particles. **Figure 4 (a)** evidently shows that ZIF particles encapsulate the surface of KCoFC particle and form hierarchically structured nanocomposites. In the subsequent elemental maps, predominant zinc signals were detected from

the exterior part of the composite, validating the ZIF-8 particles were successfully synthesized by directly growing from the surface of the KCoFC core. The cobalt and iron signals from the core crystal indicate the robust KCoFC core in the center of the composite.

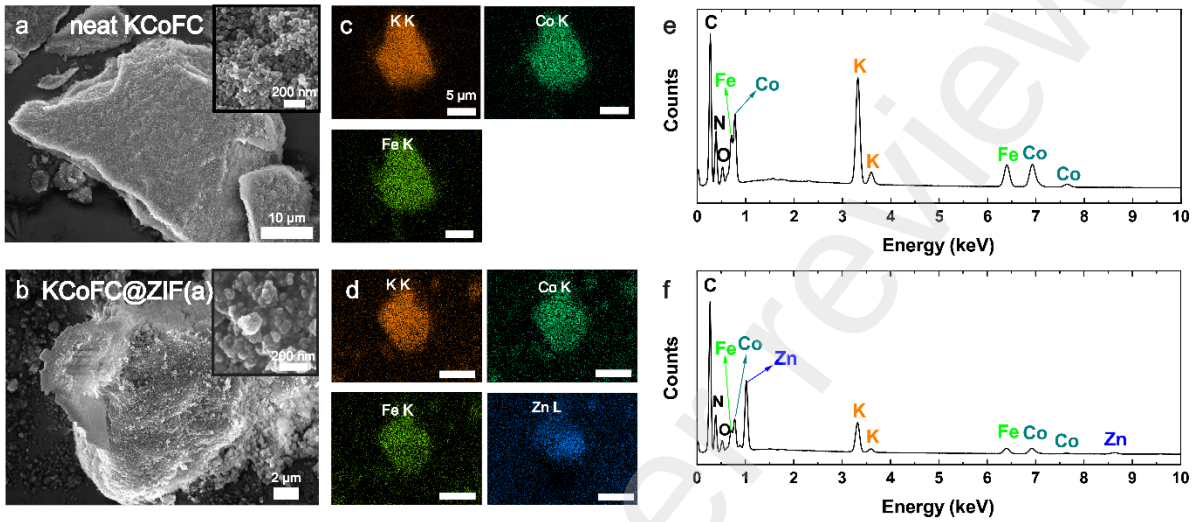

Figure 3. SEM micrographs of (a) KCoFC and (b) KCoFC@ZIF(a). EDX elemental map of (c) KCoFC, and (d) KCoFC@ZIF(a). EDX spectra show that the KCoFC particle contains K, Co, and Fe (e), whereas the KCoFC@ZIF(a) composite particle contains K, Co, Fe, and Zn (f) validating the formation of ZIF-8 crystals.

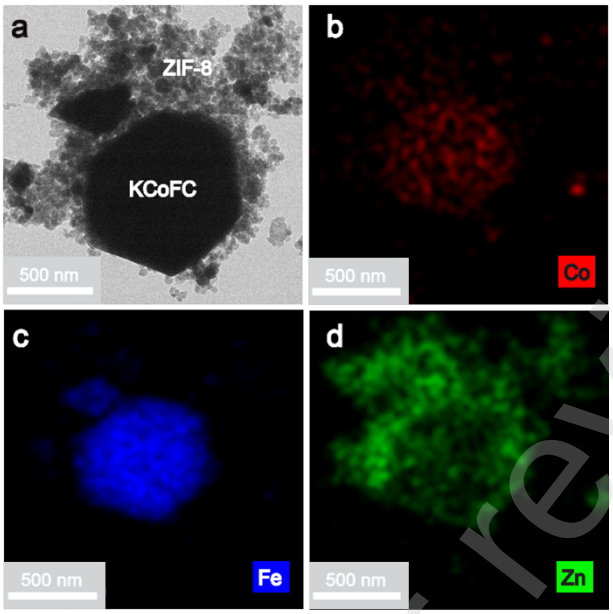

Figure 4. (a) TEM bright field image of the KCoFC@ZIF(a). **(b-d)** EDX elemental analysis shows that ZIF-8 particle is well-decorated on the surface of a KCoFC core particle.

3.2.3 Surface chemical characteristics and functional groups

Figure 5 exhibits the FTIR spectra of KCoFC and KCoFC@ZIF(a) materials. The curve of KCoFC sorbent showed a sharp peak at 2077 cm^{-1}, which indicated the stretching vibrations of the cyano groups -C≡N [30]. In addition, the band observed at 593 cm^{-1} was assigned to the stretching vibrations of Fe-CN-Co, which was confirmed by Gibert et al. [31] and Jiang et al. [32]. Meanwhile, the data of KCoFC@ZIF(a) illustrated the appearance of a few new peaks compared to the original sorbent. The bands at 759 cm^{-1} were attributed to the vibrations of a double bond between C and N atoms, while the signals at 1312 and 1146 cm^{-1} were attributed to the bending vibrations of C-N [33, 34] originated from the imidazole linker in ZIF crystals confirming the presence of ZIF in the KCoFC@ZIF composite particles.

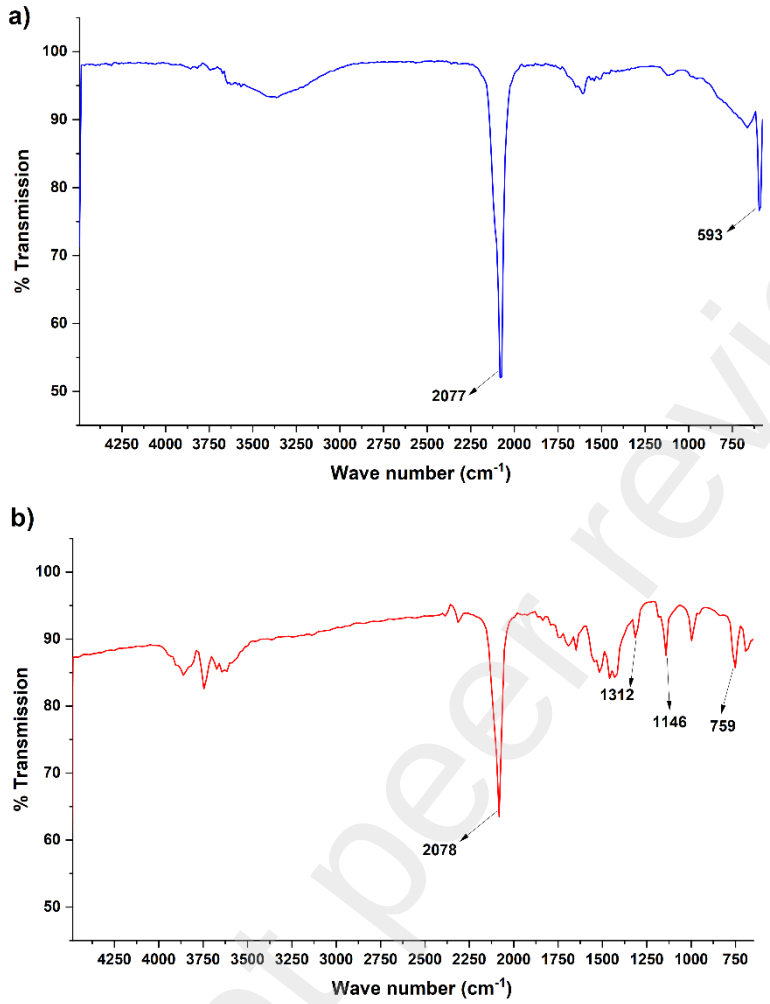

Figure 5. FT-IR spectra of (a) KCoFC and (b) KCoFC@ZIF(a) nanomaterials.

3.2.4 Surface area and pore size

Table 3 summarizes the N_2 adsorption/desorption results using the BET analysis. Notably, the surface area of KCoFC@ZIF(a) significantly increased from 62.68 m^2/g to 382.98 m^2/g, which is a 6-fold increment upon encapsulation of KCoFC with ZIF (**Figure S1**). This attributes to the highly porous structures of the ZIF phase grafted onto KCoFC particles. Meanwhile, an opposite trend was observed for the pore diameter, by which KCoFC@ZIF resulted in a significantly reduced pore size of the nanomaterial, in line with the small pore size of neat ZIF material

Table 3 Physiochemical properties of KCoFC and KCoFC@ZIF

Nanomaterial	BET Surface Area ($m^2 \cdot g^{-1}$)	Mean Pore Diameter (nm)

KCoFC	62.68	8.89
KCoFC@ZIF	382.98	3.32
ZIF	404.71	0.54

360

361 **3.2.4.1 Influence of HMIM organic linker concentration on KCoFC surface area, pore size**
362 **and crystal structure**

363 To evaluate the contribution of the metal-organic framework grafted onto the surface area and pore
364 size of KCoFC, apart from the KCoFC@ZIF composition of 1:30:5 (KCoFC@ZIF(a)), a series of
365 KCoFC composite materials with different concentration of HMIM (KCoFC@ZIF(b)-(e)) were
366 synthesized as listed in **Table 1**.

367

368 **3.2.4.1.1 Crystal Structure**

369 KCoFC@ZIF(b), which was synthesized with the highest HMIM to zinc ratio, shows higher ZIF
370 peak intensity compared to KCoFC@ZIF(a) (**Figure S2**) (*The reduced XRD patterns were*
371 *normalized by the primary characteristic peak intensity of the KCoFC which appears at 17.7°*).
372 This demonstrates that the volume of ZIF relative to KCoFC was significantly increased. In
373 contrast, the samples with lower HMIM to zinc ratios, i.e., KCoFC@ZIF(c), KCoFC@ZIF(d), and
374 KCoFC@ZIF(e), showed weaker ZIF-8 peak intensities implying that the total volume of the ZIF
375 crystal is smaller than those in KCoFC@ZIF(a). The XRD results reveal that the total volume of
376 the grafted ZIF-8 layer can be readily tuned by controlling the synthesis parameter, the HMIM to
377 zinc molar ratio.

378

379 **3.2.4.1.2 Surface area and pore size**

380 KCoFC@ZIF(a) resulted in significantly higher surface area but smaller pore diameter to KCoFC,
381 in line with the high surface area and small pore size of neat ZIF material (**Table 3**). The results
382 suggest that grafting ZIF to KCoFC increased effective surface area but reduced the mean pore
383 diameter.

384

385 **Table 4** summarizes the specific surface area and the mean pore diameter of the series of KCoFC
386 nanomaterials with different concentration of HMIM (KCoFC@ZIF(a)-(e). The trend shows that
387 the specific surface area of the nanomaterial monotonically increases with the amount of added
388 HMIM precursors. In contrast, the pore diameter was reduced as the amount of added HMIM

increases. In general, the adsorbents with larger specific surface area are favored because of the greater adsorption capacity. However, the smaller pore size may sacrifice the mass transport, adsorption kinetics, or selectivity of a certain metal ion. Hence, in order to maintain a reasonable pore size and simultaneously achieve a high specific surface area, it is critical to optimize the HMIM to zinc ratio for the ZIF synthesis. In line with this, we identify reduced HMIM composition that enables to maintain a mean pore diameter that corresponds to that of KCoFC, while obtaining an improved specific surface area than that of KCoFC as depicted in KCoFC@ZIF(d). Reducing the HMIM content further, KCoFC@ZIF(e) resulted in a significantly lower surface area. Likewise, increasing the HMIM content further, KCoFC@ZIF(b), resulted in the highest surface area but the lowest pore size.

To evaluate and establish the optimum composition of KCoFC with ZIF, and the specific influence of the larger surface area and reduced pore size towards Rb uptake, further Rb uptake performance evaluations were carried out by comparing two of the ZIF-grafted KCoFC (KCoFC@ZIF(a) and KCoFC@ZIF(d)) over neat KCoFC.

Table 4 Influence of doping amount of HMIM organic functional group on KCoFC surface area and pore size

Nanomaterial	KCoFC : HMIM : Zn molar ratio	BET Surface Area ($m^2 \cdot g^{-1}$)	Mean Pore Diameter (nm)
KCoFC	-	62.68	8.89
KCoFC@ZIF(a)	1 : 30 : 5	382.98	3.13
KCoFC@ZIF(b)	1 : 50 : 5	793.03	1.89
KCoFC@ZIF(c)	1 : 20 : 5	113.43	2.61
KCoFC@ZIF(d)	1 : 12 : 5	105.44	6.55
KCoFC@ZIF(e)	1 : 08 : 5	70.22	8.11

3.2.5 Surface zeta potential

The zeta potential analysis of the nanomaterials at pH ranges from 2 to 10 showed a trend of a more negatively charged surface with increasing pH for all three nanomaterials (**Figure 6**). The KCoFC showed a significant decrease in the surface potential as the pH was increased. A similar trend was observed by Naidu et al. [12] and the less negative surface charge of KCoFC at low pH

was attributed to the protonation of the surface functional groups. Comparatively, both of the ZIF-grafted nanomaterials, i.e., KCoFC@ZIF(a) and KCoFC@ZIF(d) showed more negatively charged surface potential than neat KCoFC at pH 2. We speculate that the surface covering ZIF layer imparts a negative charge even in highly acidic conditions.

On the other hand, at higher pH (pH 4 and above), the neat KCoFC showed a trend of a more negatively charged surface compared to both KCoFC@ZIF(a) and KCoFC@ZIF(d). To investigate the effect of ZIF on the surface potential, the pH-dependent zeta potential of neat ZIF particles were compared with the composite particle (**Figure 6**). The ZIF(a) and ZIF(d) shown in **Figure 6** refer to the pristine ZIF particles which were synthesized by the corresponding HMIM to zinc ratios without KCoFC particle substrates. The zeta potential data of both neat ZIF(a) and ZIF(d) demonstrated higher zeta potential than KCoFC in the high pH regime. Interestingly, KCoFC@ZIF(a) exhibited a similar pH-dependent zeta potential trend to that of neat ZIF(a). This result suggests that ZIF surface encapsulating layer dominates the surface charge of the composite nanomaterials. In contrast, the zeta potential of KCoFC@ZIF(d) displayed offset to more negative values compared to neat ZIF(d). This could be originated from the low volume ratio of the ZIF(d) phase relative to the KCoFC core, and thus both the KCoFC core and ZIF(d) contribute to the surface potential. Also, according to the XRD results, we expect the volume fraction of the ZIF phase in the composite to be smaller in KCoFC@ZIF(d) compared to the KCoFC@ZIF(a) and thus, the surface coverage of the ZIF layer to be smaller as well. As a result, KCoFC@ZIF(d) demonstrates a negative surface charge similar to that of KCoFC@ZIF(a) material, unlike neat ZIF(d).

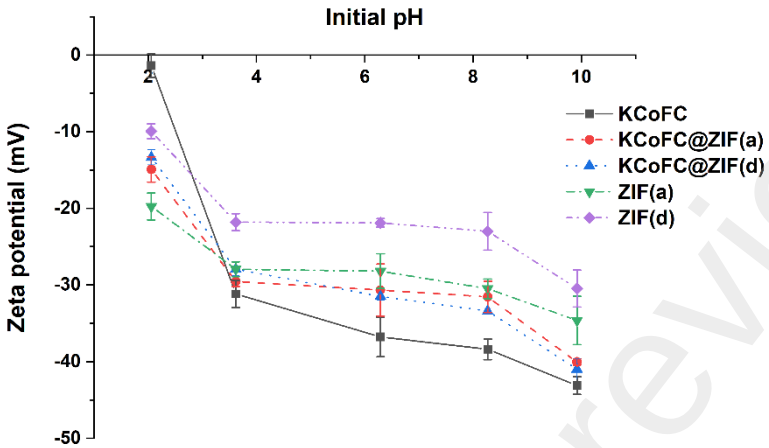

Figure 6. The trend of surface zeta charge at varied pH for nanomaterials in NaCl (1 x10^{-4} M) solution.

3.3 Performance evaluation for Rb uptake with KCoFC and KCoFC@ZIF

3.3.1 Influence of pH

Rb uptake showed only marginal changes as the solution pH was increased from 2 to 10 for all three types of nanomaterials (KCoFC, KCoFC@ZIF(a), and KCoFC@ZIF(d)) (**Figure 7**). This indicates that the solution pH did not play a significant role in influencing Rb uptake as reported by previous studies [11, 12, 35]. The results also establish the stability of the ZIF-grafted KCoFC in acidic and alkaline conditions. More importantly, Rb uptake was significantly enhanced by 5-7 times for the ZIF-grafted nanomaterial over KCoFC, following the Rb uptake order of KCoFC@ZIF(a)>KCoFC@ZIF(d)>KCoFC. It is also important to note that the neat ZIF(a) material showed only marginal Rb uptake. This clearly indicates that Rb uptake by ZIF grafted KCoFC was dominantly reliant on the presence of KCoFC as the ion exchange material. Comparing the Rb uptake of KCoFC@ZIF(a) over KCoFC@ZIF(d), although the organic linker content was 2.5 times higher for KCoFC@ZIF(a), the Rb uptake was only about 50% higher for KCoFC@ZIF(a) to KCoFC@ZIF(d). This suggests that the higher organic linker content may be an oversaturation that may not have significantly contributed to enhance Rb uptake further.

The pH-dependent zeta potential for all the nanomaterials in a RbCl (1 x10^{-4} M) solution displayed consistently higher zeta potential values than those in a NaCl (1 x10^{-4} M) solution (**Figure S3a-c**). This could be attributed to the higher capacity of Rb than Na on the surface of the nanomaterial. It was also observed that KCoFC@ZIF(d) showed a bigger shift to lower surface potential compared to KCoFC@ZIF(a) in RbCl solution, while both KCoFC@ZIF(a) and KCoFC@ZIF(d) showed closely similar negative surface potential values in a NaCl (1 x10^{-4} M) solution (**Figure 6**). This could be attributed to the higher affinity of Rb that attracts the cation onto the surface of KCoFC@ZIF(d) derived from the optimum grafting of ZIF that provides a large available specific surface area for Rb adsorption combined with KCoFC that provides the negative surface charge, resulting in charge screening effect on the surface. As such, the effective surface of KCoFC@ZIF(d) became less negatively charged.

Overall, from this trend, it can be observed that the combination of ZIF with KCoFC played a role in significantly enhancing the uptake of Rb compared to the neat KCoFC material. Further, from pH 4 onwards, Rb uptake was independent of the pH changes. In this regard, for all further Rb experiments, a pH range of 7.5-8.0 was selected in line with the pH of natural seawater.

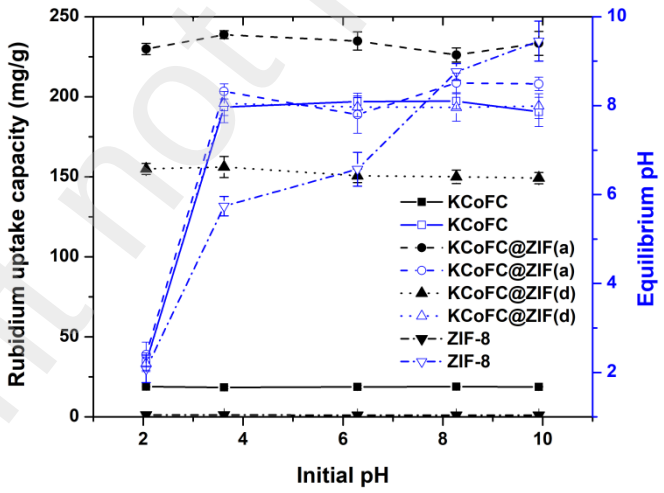

Figure 7. Influence of pH on Rb uptake by KCoFC, KCoFC@ZIFs and ZIF only material (model Rb solution = 5 mg /L; material dose = 0.25 g/L ; contact time = 24h)

3.3.2 Kinetics

Time-dependent Rb uptake of the nanomaterials were carried out to investigate the Rb uptake kinetics (**Figure 8)**. The uptake of Rb was faster for both KCoFC@ZIFs compared to the neat KCoFC material in the initial time window. Specifically, both KCoFC@ZIF(a) and KCoFC@ZIF(d) achieved 50% Rb uptake within 5h, while KCoFC required up to 12h to achieve 50% Rb uptake. It is likely that the high surface area of the ZIF-grafted KCoFC played an influencing role in proving higher surface interaction for accelerating Rb uptake. Nevertheless, in comparing the two ZIF-grafted nanomaterials, KCoFC@ZIF(d) showed better total kinetics compared to KCoFC@ZIF(a) although the surface area of KCoFC@ZIF(a) was significantly higher (**Table 4**). This could probably be associated with the smaller pore size of KCoFC@ZIF(a) that may have restricted the speed of ion diffusion (intraparticle diffusion) into the pores of the nanomaterials [36], and thereby delayed the time required for ion exchange between Rb and K in the inner cage structure of the nanomaterial, which is the dominant mechanism for Rb uptake of the nanomaterial, given the ZIF material displayed no Rb uptake as evidently established earlier (**Figure 7**). Furthermore, we speculate that the lower zeta potential in the case of KCoFC@ZIF(d) enhanced the surface electrostatic interaction with Rb cation which improved the Rb adsorption kinetics.

The Rb uptake experimental data over time were analyzed using the pseudo-first-order (PFO) and pseudo-second-order (PSO) models (**Figure S4a-c**). The results presented in **Table 5** show that the data fitted to both PFO and PSO models with R^2 above 0.90 for all three nanomaterials with a slightly better fitting for the PSO model with R^2 above 0.95. The kinetic model fitting was in accord with previous Rb studies that grafted MOF onto nanomaterials [35, 37]. The high fidelity to the PSO model implies that the Rb adsorption kinetics is predominantly determined by the chemical reaction which is dependent on the concentration of Rb and the ion exchange reaction event occurs at the KCoFC surface. Overall, the evidence here highlights that, compared to KCoFC@ZIF(a), the KCoFC@ZIF(d) was a more suitable composition for faster Rb uptake. Therefore further Rb uptake performance was carried out by comparing KCoFC@ZIF(d) and neat KCoFC.

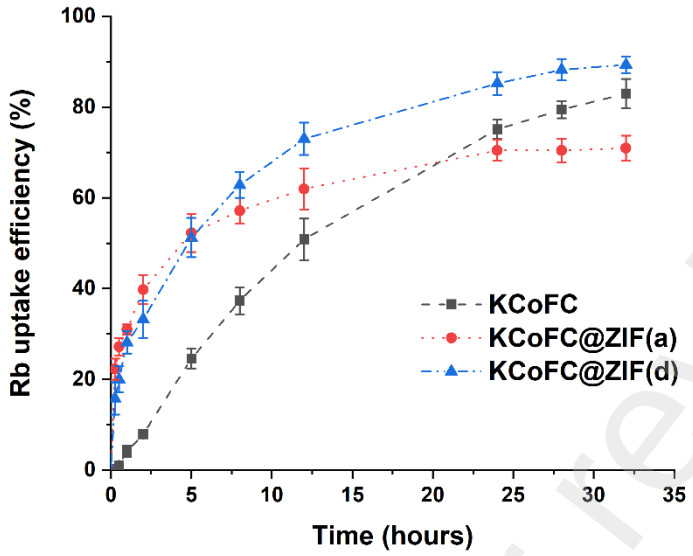

Figure 8. Rb uptake as a function of time by KCoFC and KCoFC@ZIF nanomaterials (model Rb solution = 5 mg /L; material dose = 0.05 g/L; pH= 7.0±0.5)

Table 5 Parameters and correlation coefficient (R^2) values of two applied kinetic models

	KCoFC	KCoFC@ZIF(a)	KCoFC@ZIF(d)
Pseudo-1st model parameters			
q_{e1} (mg/g)	98.07	800.84	685.56
k_1 (1/h)	0.06	0.66	0.21
R^2	0.99	0.90	0.94
Pseudo-2nd model parameters			
q_{e2} (mg/g)	147.52	869.78	772.94
k_2 (g/mg.h)	0.000277	0.00104	0.00038
R^2	0.99	0.95	0.97

3.3.3 Isotherm

As established earlier, the Rb uptake was significantly higher for ZIF-grafted nanomaterial, KCoFC@ZIF(d), compared to KCoFC. In line with this, the experimental Rb uptake data fitted to the equilibrium Langmuir model revealed that the KCoFC@ZIF(d) nanomaterial attained a maximum adsorption capacity (Q_{max}) of 1279.35 mg/g while the KCoFC attained a Q_{max} of 143.21 mg/g (**Figure 9, Table 6**). Further, the high Freundlich model correlation (R^2) of 0.98 for both

nanomaterials suggested the presence of heterogeneous surface sites and an adsorption process of Rb ions through both monolayer (chemisorption) and multilayer formations.

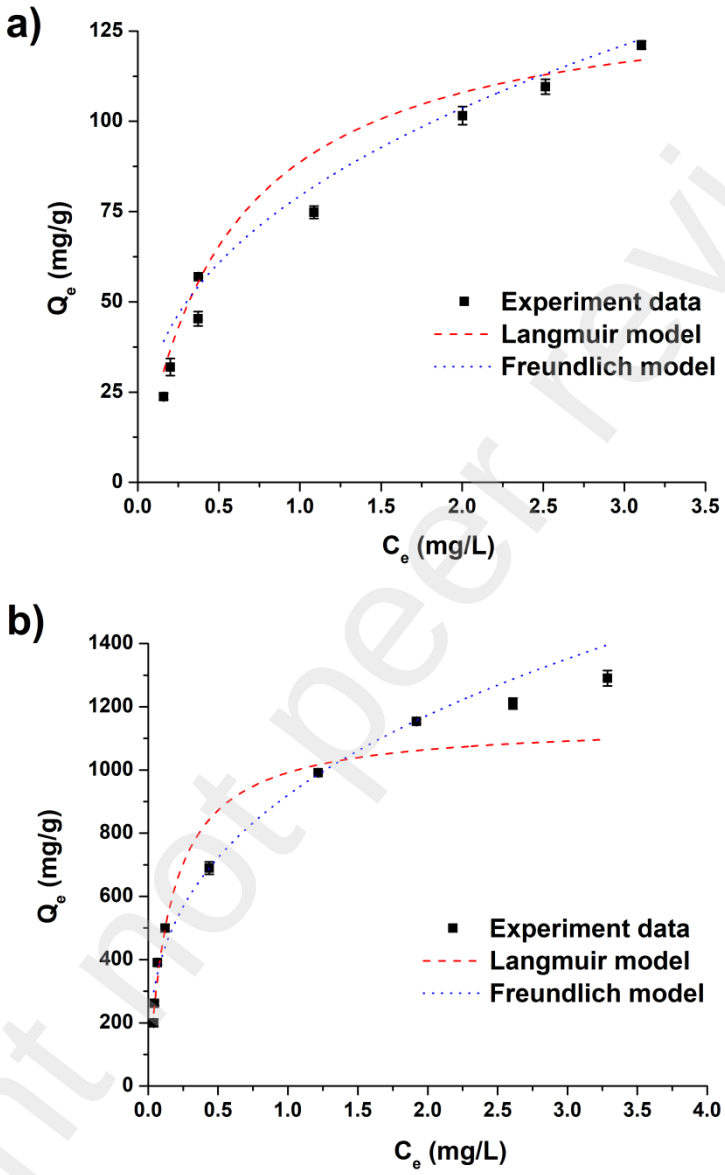

Figure 9. Rb uptake experimental data fitted to isotherm models of Langmuir and Freundlich for nanomaterials of **(a)** KCoFC and **(b)** KCoFC@ZIF(d)

Table 6 Parameters of Langmuir and Freundlich isotherm and correlation coefficient (R^2) values for nanomaterials KCoFC and KCoFC@ZIF(d)

Model Parameters	KCoFC	KCoFC@ZIF(d)
Langmuir		

K_L (L/mg)	1.32	4.42
Q_{max} (mg/g)	143.21	1279.35
R^2	0.97	0.96
Freundlich		
K_f [(mg/g)(L/mg)$^{1/n}$]	72.59	892.35
n	2.18	2.97
R^2	0.98	0.98

527

528 **3.4 Selective Rb recovery with seawater**

529 Both KCoFC and KCoFC@ZIF(d) exhibit high capacities to maintain selective Rb uptake over
530 other ions present in significantly higher concentration in seawater (**Figure 10**). Specifically,
531 minimal Na uptake (2-3%) was observed with Rb uptake, while no other ion uptake was observed,
532 in line with our previous study [11]. The high selective capacity of KCoFC and related ZIF grafted
533 KCoFC is attributed to the similar ionic radius of Rb and K that enables only Rb to enter into the
534 pores of the material and displace K inside the centre of the cubist structure. In line with this, the
535 presence of Na in high concentration over Rb, minimally affects the selective uptake of Rb. This
536 is associated to the high ion radius of Na that is unable to enter into the lattice of the material and
537 exchange with K .

538

539 However, as established in our previous study [38], KCoFC's capacity for Rb uptake was reduced
540 by around 44 - 45% in seawater (**Figure 11**). This is attributed to the presence of high potassium
541 content in seawater that reduced the capacity of K exchange with Rb due to an effect of
542 oversaturation. Likewise, KCoFC@ZIF(d) also experienced Rb uptake reduction of around 44-
543 45%, given the Rb uptake in both materials rely on the ion exchange mechanism between K and
544 Rb. However, due to the significantly higher Rb uptake capacity of KCoFC@ZIF(d) compared to
545 KCoFC, in spite of experiencing considerable Rb capacity reduction in seawater, of
546 KCoFC@ZIF(d) was still able to maintain a relatively high Rb uptake of 236.95 mg/g.

547

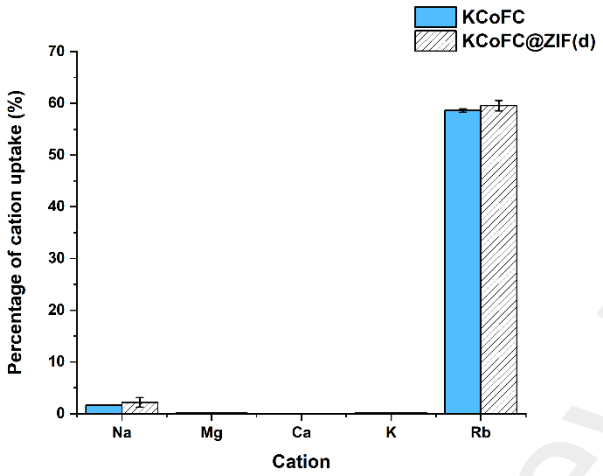

548

549 **Figure 10.** Selective Rb uptake capacity of KCoFC and KCoFC@ZIF(d) in seawater (seawater
550 spiked with 5 mg/L Rb; material dose = 0.25 g/L; pH= 7.0±0.5)

551

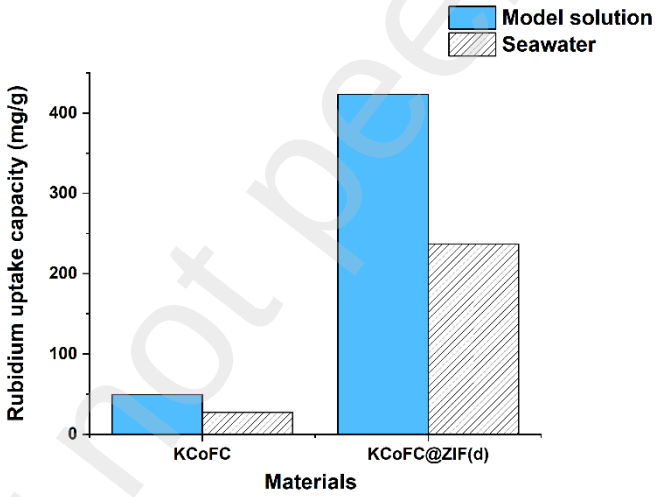

552

553 **Figure 11.** Comparison of Rb uptake capacity between KCoFC and KCoFC@ZIF(d) in model Rb
554 solution over seawater solution (seawater spiked with 5 mg/L Rb for direct comparison to model
555 solution, material dose = 0.1 g/L; pH= 7.0±0.5).

556

557 **3.5 Regeneration**

558 The regeneration and reusable capacity of the adsorbents were evaluated by repeated adsorption
559 and desorption cycles as presented in **Figure S5**. The Rb uptake capacity decreased by about 30%
560 after five regeneration cycles in both KCoFC and KCoFC@ZIF(d). This can be discernable by
561 considering the desorption capacity of the KCoFC with KCl [12]. Notably, the reduction of Rb

adsorption capacity coincides in both of the adsorbents regardless of the ZIF encapsulating layers. This observation reconfirms that the Rb adsorption and desorption are predominantly driven by the KCoFC core.

In addition, the XRD data of regenerated sorbents in **Figure S6** exhibits that after the regeneration process, some peaks related to KCoFC and ZIF crystals could still be observed in KCoFC and KCoFC@ZIF(d). It indicates that the use of KCl as the regeneration solvent did not affect the composition of both the original and composite materials. The reduced Rb capacity over each cycle is mainly attributed to the mass losses of KCOFC and KCoFC@ZIF(d) materials that are in powder form. Further work on encapsulating the material must be considered to enhance the reuse capacity of the material and its practical application in a fixed bed column.

3.6 Selective mechanism of KCoFC@ZIF for Rb uptake

The Rb uptake experiment **(Figure 7)**, evidently establishes that the amount of Rb adsorbed to the neat ZIF particles is negligible. However, the presence of the ZIF layer substantially enhanced the adsorption capacity and improved the adsorption kinetics **(Figure 8)**. On the other hand, the selectivity of Rb against other alkali metal ions was almost identical in both neat KCoFC and ZIF-grafted KCoFC, and the regeneration capacities were largely the same (**Figure 10** and **Figure S5**). Hence, it is reasonable to conclude that the ZIF layer only plays a catalytic role in the ion adsorption reaction while the Rb^+ adsorption is predominantly governed by the KCoFC.

In line with this, TEM-EDS elemental mapping on KCoFC@ZIF(a) upon Rb uptake **(Figure 12a)** showed that KCoFC@ZIF(a) consist of a core-shell structure with distinct elemental distributions. Cobalt (red) was mostly detected in the core particle region whereas the globular layer encapsulating the surface of the core particle contained mostly of zinc (blue). Interestingly, Rb (green) was predominantly scattered in the corresponding region where cobalt was detected. This high fidelity of the Co and Rb distribution complements the minimal role of ZIF phase on the Rb selective uptake.

On the basis of these observations, we propose the following adsorption mechanism depicted in **Figure 12b-c**. First, the fully hydrated Rb ions partially dehydrate at the water-ZIF interface.

According to the measurement, ZIF crystals have cavities with ~5.4 Å pore diameter which is smaller than the hydrated ionic diameter of Rb (6.58 Å), but larger than the dehydrated ionic diameter of Rb (2.96 Å) [17]. Due to the confinement effect at the ZIF cavity channels, the water molecules are repelled from the cavity, and thus, the partially solvated Rb ions can pass through the channel faster than the hydrated Rb ions in the bulk water. Indeed, density functional theory (DFT) and *ab initio* molecular dynamics simulation results on a Rb ion confined in a MoS_2 nanochannel showed a ~ 30% decrease in the coordination number indicating that some of the bonding between Rb and water molecules are broken from the first solvation shell due to the confinement effect [39]. The partially dehydrated cations lead to enhanced ion transport in the confined channel that can also improve the adsorption kinetics [40]. Subsequently, the Rb ion reaches the KCoFC@ZIF interface where the ion exchange between Rb and K occurs. The partially dehydrated Rb-H_2O clusters (**Figure 12c**) have a smaller dehydration energy barrier and consequently, it can form the inner-sphere complexes at the material surface more easily. On the other hand, fully hydrated Rb ions in the bulk water phase (**Figure 12b**) have a greater dehydration energy barrier that inhibits the adsorption [41]. This difference in energy barrier may shift the adsorption-desorption equilibrium which can determine the total adsorption capacity of the material.

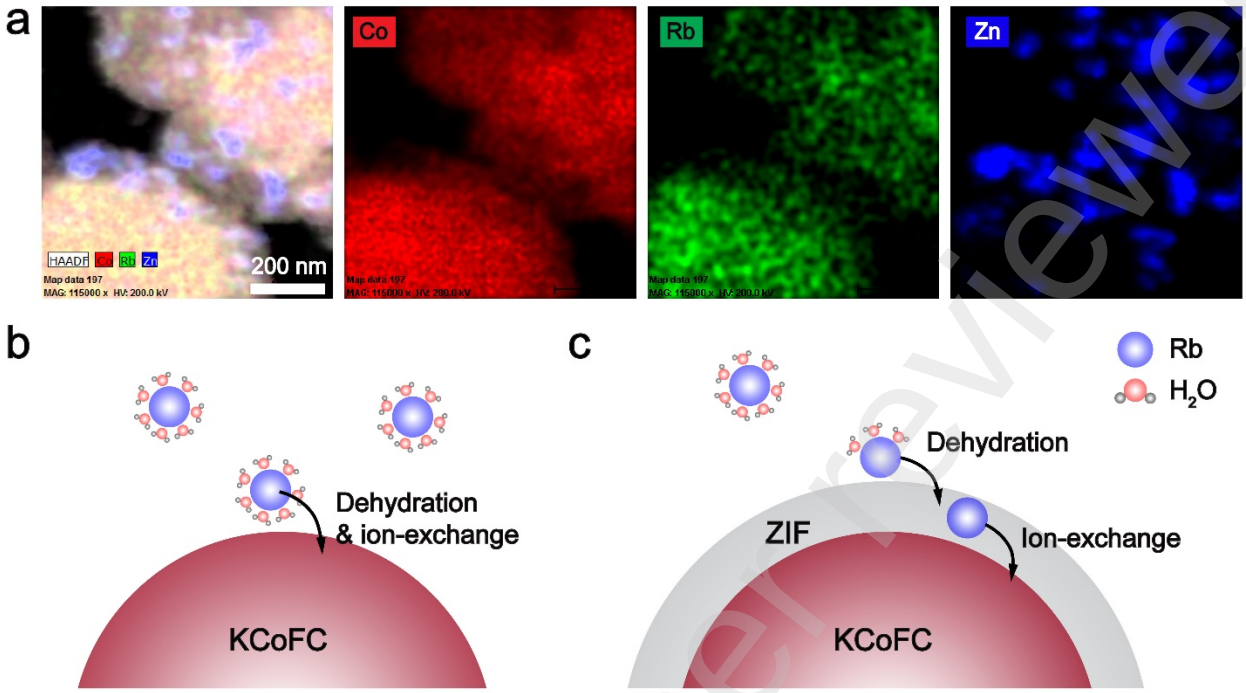

Figure 12. TEM-EDS elemental maps of KCoFC@ZIF(a) composite material after Rb adsorption (a) and proposed mechanism of the Rb adsorption to (b) KCoFC and (c) KCoFC@ZIF

At equilibrium mass, the mass of material containing only KCoFC was significantly lower by 12.4% for KCoFC@ZIF(d) compared to KCoFC (**Table 7**). The occurrence of lattice ion exchange was evident as K was released with Rb sorption in the model solution following the principle of Rb-K exchange while the release of all other elements (Co, Fe, Zn) were minimal. Nevertheless, Rb uptake and the corresponding amount of K released per gram of material was significantly higher for KCoFC@ZIF(d) compared to KCoFC. In line with the discussion based in the observation of the TEM analysis, while the ZIF in itself is inert and did not play a role in Rb uptake, the ZIF grafting onto KCoFC resulted in significantly higher surface area for KCoFC as established by the surface area analysis. It is likely, the high surface area of the material, coupled with the ZIF dehydrated Rb-H_2O cluster at the water-ZIF interface layer created higher vacant tunnel site for Rb to attach and diffuse into the pores of the KCoFC crystal lattice, thereby displacing K in the cubic centre of the structure compared to the neat KCoFC material.

Table 7 Comparison of Rb uptake and ion released by KCoFC and KCoFC@ZIF(d) at equilibrium mass

Nanomaterial	Total material mass (mg)	Mass of KCoFC in material (mg)	Rb uptake (mmol/g)	K released (mmol/g)	Zn released (mmol/g)	Co released (mmol/g)	Fe released (mmol/g)
KCoFC	25.10±0.32	25.10±0.33	0.58 ± 0.18	0.67 ± 0.25	-	0.01 ± 0.01	<0.01
KCoFC@ZIF(d)	25.10±0.32	3.05±0.03	4.95 ± 0.21	5.40 ± 0.10	0.01 ± 0.01	0.01 ± 0.01	<0.01

4. Conclusions

In order to enhance selective Rb recovery from seawater brine by potassium cobalt hexacyanoferrate (KCoFC) ion exchange nanomaterial, this study synthesized and grafted a metal organic framework, ZIF onto KCoFC. Based on the results of this study, it can be concluded that

(i) ZIF grafted KCoFC, KCoFC@ZIF was successfully synthesized as established by detail surface morphology characterization analysis;

(ii) Grafting ZIF to KCoFC increased the effective surface area but reduced the mean pore diameter. Compared to neat KCoFC (surface area = 62.68 m^2/g, pore diameter =8.89 nm), KCoFC@ZIF(a) resulted in significantly larger surface area but smaller pore size (surface area = 382.98 m^2/g, pore diameter =3.12 nm). The surface area and pore size trend of KCoFC@ZIF was influenced by the concentration of HMIM. Reducing HMIM composition to a ratio of KCoFC:HMIM:Zn 1:12:5 (KCoFC@ZIF(d)) enabled to achieve a reasonable balance in increasing the specific surface area by 63% to that of KCoFC while reducing the mean pore diameter by less than 30%;

(iii) Grafting ZIF to KCoFC played a role in enhancing Rb uptake in the order of KCoFC@ZIF(a)>KCoFC@ZIF(d)>KCoFC. Nevertheless, kinetically, the Rb uptake efficiency order was KCoFC@ZIF(d)>KCoFC>KCoFC@ZIF(a). The smaller pore diameter of KCoFC@ZIF(a) restricted Rb diffusion onto the material pores. Meanwhile the reasonable balance between high surface area and pore diameter enabled to accelerate Rb uptake for KCoFC@ZIF(d), thereby, establishing KCoFC@ZIF(d) to be an optimum composition;

(iv) Langmuir Rb sorption capacity of KCoFC@ZIF(d) was significantly higher (Q_{max} of 1279.35 mg/g), compared to KCoFC (Q_{max} was 143.31 mg/g). The kinetics data fitted well for both pseudo-first and second order model;

(v) Both KCoFC and KCoFC@ZIF(d) showed capacity to maintain high Rb selectivity over other cations present in high concentration in seawater. Compared to model Rb solution, in actual seawater solution, both the materials exhibited about 45% capacity reduction due to the presence of K in high concentration in seawater. Nevertheless, KCoFC@ZIF(d) was still able to maintain a relatively high Rb uptake of 236 mg/g in seawater;

(vi) KCoFC@ZIF(d) enabled to maintain closely similar peak structure after five consecutive operative cycles, establishing the materials regenerative capacity. Reduced Rb capacity over each cycle is mainly attributed to powder form material mass losses. Further work on encapsulating the material must be considered to enhance reuse capacity and practical application in a fixed bed column.

(vii) KCoFC core controls the Rb ion exchange and selectivity process, while the crafted ZIF layer contributes as catalytic role in increasing the surface area of the material for Rb uptake.

Acknowledgement

This work was funded by the Australian Research Council Discovery Early Career Research Award (DE200100661) and Australian-Indian Strategic Research Funding (AIRXII000019)

Reference

[1] Mineral commodity summaries 2022, Mineral Commodity Summaries, Reston, VA, 2022, p. 202.

[2] J. Jandová, P. Dvořák, J. Formánek, H.N. Vu, Recovery of rubidium and potassium alums from lithium-bearing minerals, Hydrometallurgy 119-120 (2012) 73-76. https://doi.org/https://doi.org/10.1016/j.hydromet.2012.02.010.

[3] Z.-Q. Shan, X.-Q. Shu, J.-F. Feng, W.-N. Zhou, Modified calcination conditions of rare alkali metal Rb-containing muscovite (KAl2[AlSi3O10](OH)2), Rare Metals 32(6) (2013) 632-635. https://doi.org/10.1007/s12598-013-0068-3.

[4] A. Kumar, G. Naidu, H. Fukuda, F. Du, S. Vigneswaran, E. Drioli, J.H. Lienhard, Metals Recovery from Seawater Desalination Brines: Technologies, Opportunities, and Challenges, ACS Sustainable Chemistry & Engineering 9(23) (2021) 7704-7712. https://doi.org/10.1021/acssuschemeng.1c00785.

[5] G. Naidu, S. Jeong, M.A.H. Johir, A.G. Fane, J. Kandasamy, S. Vigneswaran, Rubidium extraction from seawater brine by an integrated membrane distillation-selective sorption system, Water Research 123 (2017) 321-331. https://doi.org/https://doi.org/10.1016/j.watres.2017.06.078.

[6] J. Zhang, L. Yang, T. Dong, F. Pan, H. Xing, H. Liu, Kinetics-Controlled Separation Intensification for Cesium and Rubidium Isolation from Salt Lake Brine, Industrial & Engineering Chemistry Research 57(12) (2018) 4399-4406. https://doi.org/10.1021/acs.iecr.7b04820.

[7] G. Naidu, L. Tijing, M.A.H. Johir, H. Shon, S. Vigneswaran, Hybrid membrane distillation: Resource, nutrient and energy recovery, Journal of Membrane Science 599 (2020) 117832. https://doi.org/https://doi.org/10.1016/j.memsci.2020.117832.

[8] P. Loganathan, G. Naidu, S. Vigneswaran, Mining valuable minerals from seawater: a critical review, Environmental Science: Water Research & Technology 3(1) (2017) 37-53. https://doi.org/10.1039/c6ew00268d.

[9] B. Hu, B. Fugetsu, H. Yu, Y. Abe, Prussian blue caged in spongiform adsorbents using diatomite and carbon nanotubes for elimination of cesium, Journal of Hazardous Materials 217-218 (2012) 85-91. https://doi.org/https://doi.org/10.1016/j.jhazmat.2012.02.071.

[10] A. Cincotti, N. Lai, R. Orrù, G. Cao, Sardinian natural clinoptilolites for heavy metals and ammonium removal: experimental and modeling, Chemical Engineering Journal 84(3) (2001) 275-282. https://doi.org/https://doi.org/10.1016/S1385-8947(00)00286-2.

[11] G. Naidu, P. Loganathan, S. Jeong, M.A.H. Johir, V.H.P. To, J. Kandasamy, S. Vigneswaran, Rubidium extraction using an organic polymer encapsulated potassium copper hexacyanoferrate sorbent, Chemical Engineering Journal 306 (2016) 31-42. https://doi.org/10.1016/j.cej.2016.07.038.

[12] G. Naidu, T. Nur, P. Loganathan, J. Kandasamy, S. Vigneswaran, Selective sorption of rubidium by potassium cobalt hexacyanoferrate, Separation and Purification Technology 163 (2016) 238-246. https://doi.org/10.1016/j.seppur.2016.03.001.

[13] Y. Park, W.S. Shin, S.-J. Choi, Ammonium salt of heteropoly acid immobilized on mesoporous silica (SBA-15): An efficient ion exchanger for cesium ion, Chemical Engineering Journal 220 (2013) 204-213. https://doi.org/https://doi.org/10.1016/j.cej.2013.01.027.

[14] B. Li, H. Liu, X. Ye, S. Li, Z. Wu, Rubidium and Cesium Ion Adsorption by a Potassium Titanium Silicate-Calcium Alginate Composite Adsorbent, Separation Science and Technology 49(7) (2014) 1076-1085. https://doi.org/10.1080/01496395.2013.869230.

[15] S.H. Park, K. Kim, J.H. Lim, S.J. Lee, Selective lithium and magnesium adsorption by phosphonate metal-organic framework-incorporated alginate hydrogel inspired from lithium adsorption characteristics of brown algae, Separation and Purification Technology 212 (2019) 611-618. https://doi.org/https://doi.org/10.1016/j.seppur.2018.11.067.

[16] N. Tian, J. Wu, J. Wang, W. Dai, Development of a Novel Core–Shell Magnetic Fe3O4@CMC@ZIF-8-OH Composite with Outstanding Rubidium-Ion Capacity, Journal of Chemical & Engineering Data 64(12) (2019) 5716-5724. https://doi.org/10.1021/acs.jced.9b00708.

[17] H. Zhang, J. Hou, Y. Hu, P. Wang, R. Ou, L. Jiang, J.Z. Liu, B.D. Freeman, A.J. Hill, H. Wang, Ultrafast selective transport of alkali metal ions in metal organic frameworks with subnanometer pores, Science Advances 4(2) (2018) eaaq0066. https://doi.org/doi:10.1126/sciadv.aaq0066.
[18] X. Min, W. Yang, Y.F. Hui, C.Y. Gao, S. Dang, Z.M. Sun, Fe3O4@ZIF-8: a magnetic nanocomposite for highly efficient UO2(2+) adsorption and selective UO2(2+)/Ln(3+) separation, Chem Commun (Camb) 53(30) (2017) 4199-4202. https://doi.org/10.1039/c6cc10274c.
[19] H.N. Abdelhamid, X. Zou, Template-free and room temperature synthesis of hierarchical porous zeolitic imidazolate framework nanoparticles and their dye and CO2sorption, Green Chemistry 20(5) (2018) 1074-1084. https://doi.org/10.1039/c7gc03805d.
[20] A.F. Abdel-Magied, H.N. Abdelhamid, R.M. Ashour, X. Zou, K. Forsberg, Hierarchical porous zeolitic imidazolate frameworks nanoparticles for efficient adsorption of rare-earth elements, Microporous and Mesoporous Materials 278 (2019) 175-184. https://doi.org/10.1016/j.micromeso.2018.11.022.
[21] S. Lagergren, About the Theory of So-Called Adsorption of Soluble Substances, Kungliga Svenska Vetenskapsakademiens Handlingar 24 (1898) 1-39.
[22] G. Blanchard, M. Maunaye, G. Martin, Removal of heavy metals from waters by means of natural zeolites, Water Research 18(12) (1984) 1501-1507. https://doi.org/https://doi.org/10.1016/0043-1354(84)90124-6.
[23] I. Langmuir, The adsorption of gases on plane surfaces of glass, mica and platinum, Journal of the American Chemical Society 40 (1918) 1361–1403.
[24] H.M.F. Freundlich, Over the Adsorption in Solution, The Journal of Physical Chemistry 57 (1906) 385–471.
[25] K. Kida, M. Okita, K. Fujita, S. Tanaka, Y. Miyake, Formation of high crystalline ZIF-8 in an aqueous solution, CrystEngComm 15(9) (2013) 1794-1801. https://doi.org/10.1039/C2CE26847G.
[26] T.A. Makhetha, S.C. Ray, R.M. Moutloali, Zeolitic Imidazolate Framework-8-Encapsulated Nanoparticle of Ag/Cu Composites Supported on Graphene Oxide: Synthesis and Antibacterial Activity, ACS Omega 5(17) (2020) 9626-9640. https://doi.org/10.1021/acsomega.9b03215.
[27] P.-F. Liu, K. Tao, G.-C. Li, M.-K. Wu, S.-R. Zhu, F.-Y. Yi, W.-N. Zhao, L. Han, In situ growth of ZIF-8 nanocrystals on layered double hydroxide nanosheets for enhanced CO2 capture, Dalton Transactions 45(32) (2016) 12632-12635. https://doi.org/10.1039/C6DT02083F.
[28] J. Yang, X. Luo, T. Yan, X. Lin, Recovery of cesium from saline lake brine with potassium cobalt hexacyanoferrate-modified chrome-tanned leather scrap adsorbent, Colloids and Surfaces A: Physicochemical and Engineering Aspects 537 (2018) 268-280. https://doi.org/https://doi.org/10.1016/j.colsurfa.2017.10.015.
[29] Y. Ru, S. Zheng, H. Xue, H. Pang, Potassium cobalt hexacyanoferrate nanocubic assemblies for high-performance aqueous aluminum ion batteries, Chemical Engineering Journal 382 (2020) 122853. https://doi.org/https://doi.org/10.1016/j.cej.2019.122853.
[30] Y. Bondar, Y. Olkhovyk, S. Kuzenko, Nanocomposite adsorbent based on polyacrylonitrile fibers for rapid and selective removal of Cs radionuclides, Journal of Radioanalytical and Nuclear Chemistry 330(3) (2021) 1221-1231. https://doi.org/10.1007/s10967-021-08014-1.
[31] O. Gibert, C. Valderrama, M. Peterkóva, J.L. Cortina, Evaluation of Selective Sorbents for the Extraction of Valuable Metal Ions (Cs, Rb, Li, U) from Reverse Osmosis Rejected Brine, Solvent Extraction and Ion Exchange 28(4) (2010) 543-562. https://doi.org/10.1080/07366299.2010.480931.
[32] C. Jiang, J. Ni, G.-P. Jin, Magnetic potassium cobalt hexacyanoferrate nanocomposites for efficient adsorption of rubidium in solution, Separation and Purification Technology 296 (2022). https://doi.org/10.1016/j.seppur.2022.121383.
[33] X. Yan, Y. Li, X. Hu, R. Feng, M. Zhou, D. Han, Enhanced adsorption of phenol from aqueous solution by carbonized trace ZIF-8-decorated activated carbon pellets, Chinese Journal of Chemical Engineering 33 (2021) 279-285. https://doi.org/10.1016/j.cjche.2020.06.027.

[34] J. Yao, R. Chen, K. Wang, H. Wang, Direct synthesis of zeolitic imidazolate framework-8/chitosan composites in chitosan hydrogels, Microporous and Mesoporous Materials 165 (2013) 200-204. https://doi.org/10.1016/j.micromeso.2012.08.018.
[35] N. Tian, Y. Dai, Q. Liu, W. Dai, Highly efficient capture of rubidium ion by a novel HS-Fe3O4@MIL-53(Al) composite material, Polyhedron 166 (2019) 109-114. https://doi.org/10.1016/j.poly.2019.03.052.
[36] W. Liu, Y. Zhang, S. Wang, L. Bai, Y. Deng, J. Tao, Effect of Pore Size Distribution and Amination on Adsorption Capacities of Polymeric Adsorbents, Molecules 26(17) (2021). https://doi.org/10.3390/molecules26175267.
[37] Y. Wang, K. Li, D. Fang, X. Ye, H. Liu, X. Tan, Q. Li, J. Li, Z. Wu, Ammonium molybdophosphate/metal-organic framework composite as an effective adsorbent for capture of Rb+ and Cs+ from aqueous solution, Journal of Solid State Chemistry 306 (2022). https://doi.org/10.1016/j.jssc.2021.122767.
[38] G. Naidu, S. Jeong, Y. Choi, M.H. Song, U. Oyunchuluun, S. Vigneswaran, Valuable rubidium extraction from potassium reduced seawater brine, Journal of Cleaner Production 174 (2018) 1079-1088. https://doi.org/10.1016/j.jclepro.2017.11.042.
[39] C. Zhan, Y. Sun, F. Aydin, Y.M. Wang, T.A. Pham, Confinement effects on the solvation structure of solvated alkaline metal cations in a single-digit 1T-MoS2 nanochannel: A first-principles study, The Journal of Chemical Physics 154(16) (2021) 164706. https://doi.org/10.1063/5.0047554.
[40] A. Sugahara, Y. Ando, S. Kajiyama, K. Yazawa, K. Gotoh, M. Otani, M. Okubo, A. Yamada, Negative dielectric constant of water confined in nanosheets, Nature Communications 10(1) (2019) 850. https://doi.org/10.1038/s41467-019-08789-8.
[41] S.S. Lee, P. Fenter, K.L. Nagy, N.C. Sturchio, Real-time observation of cation exchange kinetics and dynamics at the muscovite-water interface, Nature Communications 8(1) (2017) 15826. https://doi.org/10.1038/ncomms15826.